Versatile electrochemical cell for Li-/Na-ion batteries and high-throughput setup for combined *in operando* X-ray diffraction and absorption spectroscopy

Authors

Jonas Sottmann[a]*, Roberto Homs-Regojo[b], David Wragg[a], Helmer Fjellvåg[a], Serena Margadonna[ac] and Hermann Emerich[b]*

[a]Department of Chemistry, University of Oslo, P.O. Box 1033, Oslo, 0315, Norway

[b]Swiss–Norwegian Beamlines, European Synchrotron, 71 Rue des Martyrs, Grenoble, 38043, France

[c]College of Engineering, Swansea University, Swansea, SA1 8EN, United Kingdom

Correspondence email: jonas.sottmann@smn.uio.no; ermano@esrf.fr

Synopsis *in operando* set-up, that enables deep insights into working mechanisms of electrode materials under working conditions using quasi-simultaneous XRD, XANES and EXAFS analysis, is described.

Abstract A fundamental understanding of de/intercalation processes (single phase *vs.* two-phase), structural stability and voltage-composition profiles is pivotal for optimization of electrode materials for rechargeable metal-ion batteries. A fully operational set-up (electrochemical cells, sample changer and interfacing software) that enables combined quasi-simultaneous X-ray diffraction (XRD) and absorption (XANES and EXAFS) measurements coupled with electrochemical characterization *in operando* conditions is presented. Combined XRD, XANES and EXAFS analysis provide a deep insight into the working mechanisms of electrode materials as shown for the high voltage Li insertion cathode material $LiMn_{1.5}Ni_{0.5}O_4$ and the high capacity sodium conversion anode material Bi_2S_3. We also demonstrate that the cell design can be used for in house XRD characterization. Long term cycling experiments on both Li and Na electrode materials prove the hermeticity and chemical stability of the design as a versatile *in operando* electrochemical cell.

Keywords: *in situ* methods; batteries; electrochemical cells; powder diffraction; X-ray absorption spectroscopy.

1. Introduction

Rechargeable metal-ion batteries are central to our way of life and the technology is likely to become even more important as the use of renewable energy increases. Lithium-ion batteries (LIBs) have conquered the market for portable devices and the growing electric vehicle sector. Ambient temperature rechargeable battery technology also offers good opportunities for stationary energy storage which is required to stabilize electric grids with an increasing share of intermittent renewable energy sources. Limited Li resources might make sodium-ion batteries (SIBs) a suitable technology for large-scale stationary energy storage where lower energy density is less a concern than cost (Berg *et al.*, 2015, Slater *et al.*, 2013, Palomares *et al.*, 2012). While the LIBs have been intensely investigated since the early 1960s, huge research efforts are currently undertaken in order to find suitable SIB materials.

Understanding the working mechanism of an electrode material at the atomic scale is fundamental to develop better materials and the key to this is the investigation *in situ* during operation (also called *in operando*). During preparation of samples for *ex situ* characterization the highly reactive electrode species may have relaxed, been short circuited or contaminated with atmospheric species. Further, a limited number of samples of the same material at different charge states for *ex situ* characterizations may miss a lot of fine details between the sampling points. *In operando* characterization avoids these problems: short-lived intermediates and nonlinearities in behavior can be resolved; different charge rates can be applied and time dependent processes under non-equilibrium conditions can be studied; long term cycling experiments become practically feasible and activation/fading processes can be investigated. In recent decades *in operando* (*in situ*) diffraction, spectroscopy and other advanced characterization techniques have substantially contributed to our understanding of electrode systems (Harks *et al.*, 2015, Peterson & Papadakis, 2015, Sharma *et al.*, 2015, Nelson Weker & Toney, 2015, Amalraj & Aurbach, 2011, Marco & Veder, 2010, McBreen, 2008, Novák *et al.*, 2000, Morcrette *et al.*, 2002).

Lithiation/sodiation of electrode materials can involve phase transitions, the formation of solid solutions or conversion reactions (Tarascon & Armand, 2001). XRD and total scattering are perfectly suited to pin-down the nature of the insertion process (single *vs.* two-phase), its associated structural changes (atomic arrangement, volume) and its reversibility upon cycling. These are critical factors for battery performance *i.e.* the voltage profile and capacity retention. Insertion and deinsertion of ions can for example, follow different routes (Sottmann, Bernal*, et al.*, 2016) and mechanisms may vary depending on the initial composition (degree of order (Samarasingha *et al.*, 2016), different water content (Sottmann, Bernal*, et al.*, 2016), *etc.*), particle size (Sottmann, Herrmann*, et al.*, 2016) and applied charge rate (Tang *et al.*, 2010).

In operando X-ray absorption spectroscopy (XAS) including X-ray absorption near-edge structure (XANES) and extended X-ray absorption fine-structure (EXAFS) have increasingly been used to study the changes in electronic and local structure of electrode materials, associated with the redox reactions taking place in batteries (Yamamoto *et al.*, 2014, Giorgetti, 2013, Deb *et al.*, 2007). The XANES portion of the spectrum at different states of charge provides information about the oxidation state variations of specific elements and their site symmetries. EXAFS probes the short range order in the vicinity of specific elements and enables us to follow the evolution of inter-atomic distances in the electrode materials as a function of charge state. EXAFS can also be used to analyze the size and shape of nanoparticles as well as the surface morphology and disorder of 1-2 nm clusters (Frenkel *et al.*, 2011). XAS methods are well established for insertion electrodes (Bleith *et al.*, 2015, Lv *et al.*, 2013, Ito *et al.*, 2011, Balasubramanian *et al.*, 2001, Dominko *et al.*, 2009, Nakai *et al.*, 1999) and were central in the elucidation of reaction mechanisms in conversion materials (Permien *et al.*, 2016, Hu *et al.*, 2013, Lowe *et al.*, 2013).

The electrochemical response of a battery material is intimately linked to its structural and electronic changes upon cycling. Combined quasi-simultaneous *in operando* XRD/PDF and XAS measurements coupled with electrochemical characterization are an extremely powerful tool to achieve a deep understanding of the electrochemical reaction and degradation mechanisms of electrode materials during continuous cycling.

Several types of X-ray transparent electrochemical cells have been proposed (*cf*. Table 1). The designs can be separated into three main types: (1) flexible disposable - pouch cells sometimes also referred to as “coffee bag” cells; (2) solid disposable – modified coin cells; (3) solid reusable cells - “Swagelock type”. Some cells are used in reflection configuration (Bragg-Brentano geometry) which is commonly available in home lab X-ray diffractometers. Others are used in transmission configuration (Debye-Scherrer geometry) which requires high energy X-ray sources that enable full penetration of the battery stack (electrodes, electrolyte, separator and Al/Cu current collector foil). The tunable energy and high brilliance of synchrotron radiation allow for structural information collected over a wide q-range, minimization of fluorescence problems (which arise *e.g.* in samples containing Fe when using Cu radiation) and investigation of time dependent processes. Operating in transmission geometry has the advantage of sampling the entire depth of the working electrode instead of a surface layer with an angle and composition dependent depth. Further, in case of full cells structural information could be obtained simultaneously on both anode and cathode materials. Analysis of complex powder diffraction patterns containing multiple components and phases can be realized using pattern fitting programs, such as TOPAS (Bruker AXS). Electrochemical cells for *in operando* XAS characterization (*cf*. Table 1) are similar to the cells used for XRD. For most elements XAS spectra are obtained in transmission geometry, though for lighter elements fluorescence mode (reflection geometry) is preferable because of the weaker penetration of the lower energy X-rays.

Despite the many electrochemical cell designs for *in operando* synchrotron XRD/XAS only a few automated sample-changers which allow for efficient use of beamtime were reported (*cf*. Table 1).

Table 1 In operando electrochemical cell designs.

Reference	pouch cell	coin cell	Swage-lock	mode (1)	source (2)	XAS	Sample changer
this work, SNBL cell			x	T	S,H	x	12 cells
(Herklotz *et al.*, 2016)		x		T	S		8 cells
(Bleith *et al.*, 2015)			x	T	S	x	
(Shen *et al.*, 2014)			x	R	H		
(Villevieille *et al.*, 2014)	x			T,R	S,H	x	
(Wilson *et al.*, 2014)	x			R	H		
(Brant *et al.*, 2013)			x	T	S		
(Herklotz *et al.*, 2013)			x	T	S		4 cells
(Borkiewicz *et al.*, 2012)			x	T	S	x	6 cells
(Shui *et al.*, 2012)			x(Be)	R	H		
(Rhodes *et al.*, 2011)		x		R	H		
(Leriche *et al.*, 2010)				T,R	S,H	x	
(Shin *et al.*, 2008)		x		T	S		
(Rosciano *et al.*, 2007)	x			T	S		32 cells
(Baehtz *et al.*, 2005)			x	T	S		
(Nikolowski *et al.*, 2005)			x	T	S		
(Deb *et al.*, 2004)			x	T		x	
(Braun *et al.*, 2003)			x(Be)	T	S	x	
(Ronci *et al.*, 2000, 2001)			x	R	S		
(Farley *et al.*, 1999)			x	T	S	x	
(Gérand *et al.*, 1999)	x			T	H		
(Asahina *et al.*, 1997)		x		R	H		
(McBreen *et al.*, 1997)			x	T		x	
(Richard *et al.*, 1997)		x(Be)		R	H		
(Gustafsson *et al.*, 1992)	x			T	H		
(McBreen *et al.*, 1987)			x	T		x	
(Fleischmann *et al.*, 1986)	x(Be)		x(Be)	R	H		
(Dahn *et al.*, 1982)			x(Be)	R	H		

(1) T for transmission mode, R for reflection configuration

(2) S for synchrotron and H for home lab X-ray source

In this report, we present a fully operational set-up (electrochemical cells, sample changer and interfacing software) that enables quasi-simultaneous X-ray diffraction (XRD) and absorption

(XANES and EXAFS) measurements at *in operando* conditions at the Swiss Norwegian Beam Lines (SNBL) at the European Synchrotron (ESRF), Grenoble, France. The electrochemical cells (SNBL cells) have also been used for *in operando* home lab XRD characterization. The SNBL cell is highly hermetic, stable with respect to the chemicals used in LIB and SIB technology, robust, reusable, easy to clean, and easy to mount/change in the automated sample changer. Good comparability between electrochemical performance in coin cells and the proposed cell was obtained due to the closeness in battery assembly (including electrolyte filling and applied pressure). Fast data collection and the automated sample changer which fits up to 12 easily changeable cells cycled at the same time ensure efficient use of synchrotron beamtime. Interfacing software can trigger a sequence of XRD/XAS measurements based on the electrochemical state (capacity, voltage, cycle number) of the batteries which is continuously read in real time and linked to the synchrotron measurements. The functionality of the SNBL cell for both, combined synchrotron XRD/XAS, as well as home lab XRD *in operando* characterization is validated by experiments based on a high voltage Li insertion cathode material $LiMn_{1.5}Ni_{0.5}O_4$ and a high capacity sodium conversion anode material Bi_2S_3.

2. Implementation

2.1. Cell design

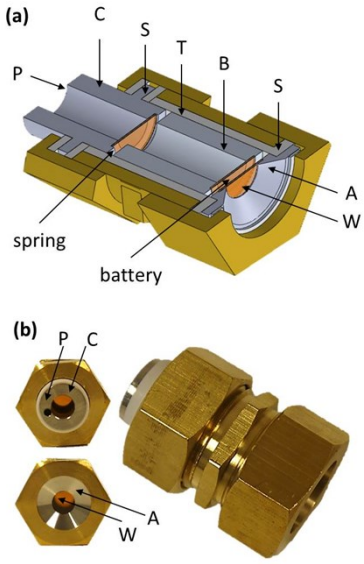

Figure 1 (a) Schematic drawing and (b) photograph of the SNBL cell. Pistons **A**, **B** and **C**, sealing **S**, Teflon cylinder **T**, X-ray transparent window made of Kapton **W** and banana socket **P**.

A schematic drawing of the SNBL cell is shown in Fig. 1. Metallic pistons with Kapton windows (**W**) are pressed on the cathode and anode which are separated by electrolyte-soaked glass fiber (Whatman, GF/C). The Kapton window could also be replaced by rigid conductive windows made out of dense glassy carbon (Sigradur-(G)) as recently suggested (Herklotz *et al.*, 2016, Borkiewicz *et al.*, 2015). A Teflon cylinder (**T**) with an inner diameter of 18 mm is used to host the battery and the pistons

because it is chemically inert and electrically insulating. Teflon is also used to hermetically seal the electrochemical cell by pressing the metal to Teflon contacts (**S**). The working electrode is coated on or contacted to the Al foil (Cu foil for Li anodes) and then placed on piston **A** which is closest to the beam exit. The mass loading of the electrodes has to be optimized depending on the materials scattering power. Usually half cells are assembled where the counter electrode is metallic Li or Na, which can be filled in the cavity between the Kapton window and the surface of piston **B**. A spring washer between pistons **B** and **C** ensures enough pressure for good electrical and ionic contact. A flow chart of the assembly procedure is shown in Fig. S1. Piston **C** is electrically insulated from the outer casing and is used as the negative contact. The outer casing serves as positive contact. The X-ray window (**W**) has an 8 mm diameter and an opening angle of 120 degrees.

2.2. Automated sample changer

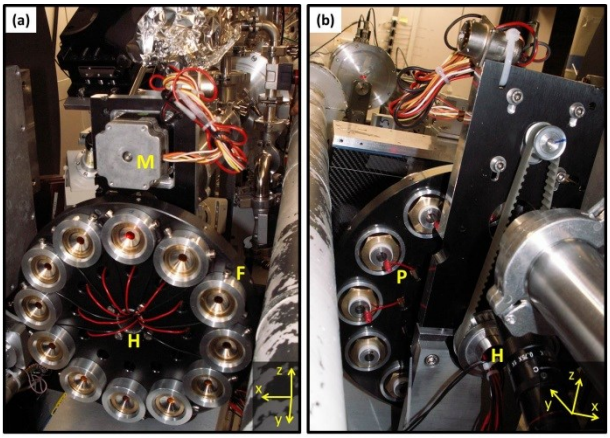

Figure 2 Photographs of (a) front and (b) rear of the of the automated sample changer. Stepper motor **M**, fixing screw **F**, hollow hub of the wheel **H** and banana socket **P**.

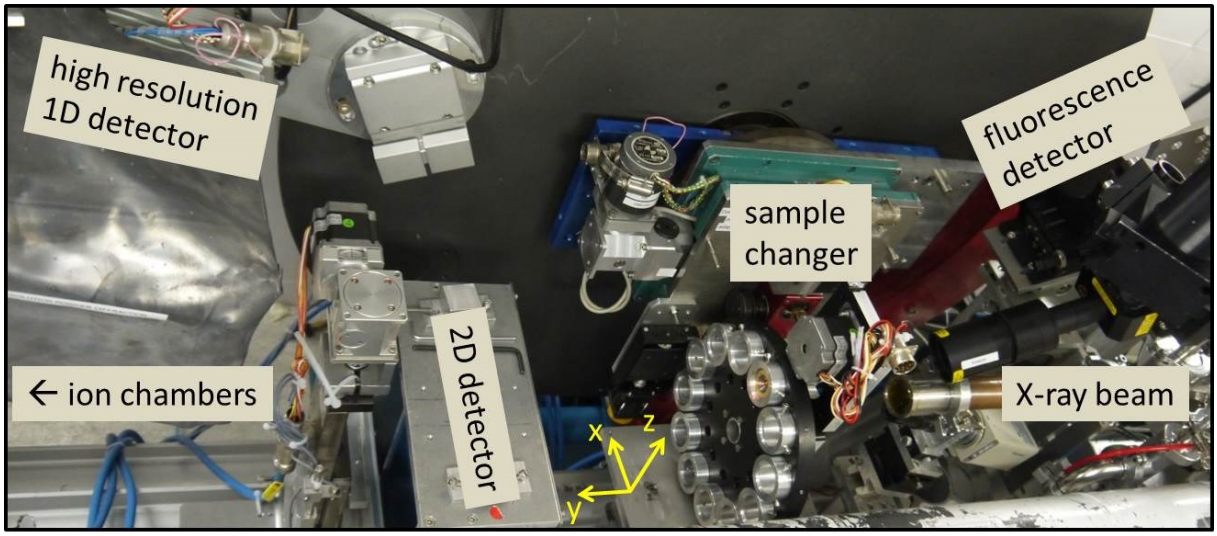

Figure 3 Photograph of the set-up at SNBL BM01B. Ion chamber and fluorescence camera are not visible but their positions are indicated. The electrical connections to cells are missing in the photograph.

The automated sample changer is designed as a vertical wheel with 12 evenly spaced sample housings (Fig. 2). The wheel is made of a nonconductive rigid plastic (Delrin) in which metallic cell holders are placed. The cell holders are cylinders featured with a reference edge with respect to which the cells are aligned and fixed by a screw (**F**). The SNBL cells are connected to a multi-channel galvanostatic battery cycler (Bat-Small, Astrol Electronic AG) by wires fixed to the cell holder and connected to piston **C** using banana plugs (**P**), respectively. In this way the SNBL cells are easily changed using the fixing screw (**F**) and the banana plug (**P**). The cables are removed from the beam path by guiding them through the hollow hub of the wheel (**H**). The cells can be alternated by rotating the wheel in steps of 30 degrees using a stepper motor (**M**) that is connected to the axle via a timing belt to reduce the torque. The cables are flexible enough to allow for a 360 degree rotation of the wheel. The sample changer is mounted on a *xyz*-stage (directions indicated in Fig. 3, *y* being parallel to the beam). The positon of the cell in the *xz*-plane is aligned using an X-ray camera and remains fixed during the entire experiment. For the XRD measurements it is important that the cell (*i.e.* the active material) is in the center of the diffractometer which is also referred to as the zero position. The zero position can be found by optimizing the scattering intensity of a high angle Bragg reflection from the metal foil by varying the *y-position*. It is reasonable to optimize the position based on an Al Bragg reflection since Al foil and electrode are in direct contact and are both thin with respect to the distance to the detector. Accurate sample-detector distance-centering of the cells along *y* is required for data collection when using the High Resolution Powder Diffraction (HRPD) set-up in order to avoid large zero errors and loss in scattering intensity. In this case the *y* position of each cell has to be determined individually and can be programmatically set using the motorized high precision *xyz*-stage during the measurement. In contrast, if a 2D detector is used, precise positioning of the cells along *y* prior to the experiment is not required as shown below. The distance between the center of the diffractometer and the 2D detector is usually set to about 40 cm. Fig. S2a shows the diffraction profiles of Al foil in a cell mounted in the zero position and displaced along *y* in 1 mm steps in the range of ±3 mm (< 1 % of the distance to detector) from the center. An angle dependent shift of the diffraction pattern is clearly noticeable. Fig. S2b shows the same diffraction profiles corrected for the displacement error prior to data reduction with pyFAI (Ashiotis *et al.*, 2015). For this purpose the distance parameter was modified iteratively in pyFAI (here by -3, -2, -1, +1, +2 and +3 mm) until the Al peak of the cell in zero and displaced positions matched. After this treatment, peak positons, shape and intensities overlap closely. This procedure can also be applied to the set of cells in the sample changer which was centered using one reference cell at the beginning of the experiment. The diffraction profile of the reference cell with Al or Cu foil is then used to determine the corrected distance parameter for the

other cells using pyFAI. For about 70 cells the average displacement with respect to the reference cell was 0.7 ± 0.6 mm with a maximum distance of 2.3 mm. This is in good agreement with a different experiment where the positions of 10 cells were adjusted prior to data collection (displacement of 0.6 ± 0.5 mm in average). Using this procedure the time consuming sample-detector distance-centering of each cell can be avoided and dead time due to the slow movement of the high precision *xyz*-stage is minimised. These time savings together with the faster data acquisition times using a 2D detector allow for an efficient use of experimental time. Another advantage is that the SNBL cells can be changed easily and rapidly without disrupting the measurement of other cells. Therefore, not all cells that are to be investigated have to be mounted in the sample changer prior to the start of the experiment. The 12 sample housings allow for flexibility in the choice of materials/conditions and high-throughput.

2.3. Setup at SNBL and beamline specifications

In operando quasi-simultaneous powder XRD and XAS can be performed at the Swiss-Norwegian Beam Lines (SNBL), BM01B, at the European Synchrotron (ESRF). The set-up at the beamline is shown in Fig. 3. XRD experiments on the SNBL cell are performed in transmission mode. The X-ray beam penetrates the whole assembly and Bragg peaks relative to the different parts of the electrochemical cell will be visible in the diffraction profiles, allowing for simultaneous characterization of both cathode and anode materials in a full cell. For the XRD measurements it is possible to choose between a 1D high resolution powder diffractometer with 6 Si-111 analyzer crystals and a Dexela 2923 CMOS 2D detector (Abdala *et al.*, 2014) with high counting statistics. With the 2D detector sufficient data quality is obtained in less than a minute, while it takes about 15 min for a high resolution scan in the angular range (2Θ) of 5.5 to 25 degrees with poor counting statistics. For efficient use of the beamtime it is therefore recommended to use the high resolution detector only in selected regions where splitting of narrow Bragg reflections needs to be resolved. Absorption (fluorescence) problems during XRD data collection can be minimized by tuning the beam energy using the monochromator set-up. For diffraction measurements a wavelength of around 0.5A is typically used in combination with the powder monochromator. The HRPD is optimized for this wavelength. In contrast, using the 2D detector, different energies from 18 to 70keV can be utilized in combination with the Exafs monochromator. Furthermore, the access to high energies permits the use of Total Scattering techniques (Abdala *et al.*, 2014). Normally the wavelength is determined using a silicon powder standard on the HRPD. To obtain the positional parameters of the 2D detector one collects a data set on a LaB_6 (NIST) standard which is refined in turn with a sub-functionality of pyFAI using the wavelength from the silicon measurement.
Once the calibration is done, the set-up can be moved in the *xz*-plane before each measurement to reduce preferential orientation effects on XRD and inhomogeneity effects on the quality of the EXAFS measurements for each individual cell (see below).

XAS measurements can be done simultaneously for transmission, fluorescence and reference data using the ion chambers and the single-element fluorescence drift detector, respectively. The Si-(1 1 1) channel-cut monochromator provides a wide energy range from 4.8 to 80 keV meaning that the lightest accessible element is Ti with an edge energy of ~5 keV. The second crystal is usually detuned to about 65 % peak intensity to reduce higher harmonics. Using the ion chambers the gas filling has to be adjusted for the energy range investigated and it is therefore only possible to measure edges over a limited energy window. The fluorescence detector is used for light elements (up to about 20 keV). A XANES measurement of the Ni K-edge (8.3 keV) takes about 4 min, while an EXAFS measurement takes about 7 min. For XANES measurements of the Bi L3-edge (13.4 keV) or Mo K-edge (20.0 keV) 2 min are sufficient when running in transmission mode.

The number of cells that can be measured concurrently to allow for sufficient data point density for both XRD and XAS depends on the measurement time and the charge rate. If the charge rate is C/10 (corresponding to one dis-/charge in 10 h) up to 8 cells can be measured in parallel with about 25 XRD (1 min per scan) and XAS (2 min per measurement) data sets per dis-/charge step.

2.4. Software implementation

The electrochemical measurements are automatically controlled by the battery cycling system from Astrol Electronic AG (using a Bat-Small battery cycler) which features easy programming and flexibility while running**.** A custom-made python program (available from the authors on request) fetches the current values (time, voltage, specific capacity) of each running measurement channel and sends them continuously (via a device server) to the computer from where the different X-ray measurements are coordinated. In an executable bash-like script the cell positions (rotation and *xyz*-position), the corresponding measurement sequence (XRD (2D, 1D), XAS (XANES, EXAFS, at different edges)) and a condition for when a given cell should be measured are defined for each individual cell. Possible conditions are that the cell should be measured in given time, voltage or specific capacity steps. A queuing system is implemented if the conditions are simultaneously fulfilled for several cells. Different priorities can also be assigned to each cell so that if a certain condition is fulfilled for two cells simultaneously it is the higher priority one which will be measured first. The electrochemical information is automatically linked to the XRD and XAS data and registered in a common data-s log file which makes this implementation very user-friendly for further data analysis.

2.5. In operando XRD in home lab

The SNBL cell can also be used for *in operando* XRD in a home lab. XRD measurements were performed in transmission mode on a Bruker D8 A25 powder diffractometer with Mo Kα1, Kα2 (λ_1= 0.7093 Å, λ_2= 0.71359 Å) radiation, focusing mirror optics and Lynxeye XE high energy detector. One scan of sufficient quality in the angular range of 7 to 36 degrees took 20 min and a charge rate of

C/10 was applied. Due to the long data acquisition time the *in operando* home lab XRD characterization is limited to low charge rates.

2.6. Parametric refinements

All profile fittings and Rietveld refinements were performed using TOPAS V5 (Bruker AXS). For each powder pattern zero-shift, background (Chebychev polynomial 8-13 terms), unit cell parameters, peak-profile parameters for the individual phases, as well as their scale factor, were refined. Broad background features due to amorphous material (glass fiber, carbon black, binder, Kapton *etc.*) were fitted with broad peaks with refined position, Gaussian broadening and intensity. Reflections from the textured Al foil were fitted for each individual powder pattern using a structureless phase with the lattice parameter and space group of Al metal (a = 4.05 Å, Fm-3m). Spot-like irregular reflections from the Li/Na metal were fitted with individual peaks (refining position, width and intensity) for the individual powder patterns. Each series of powder patterns was refined in parallel as a single dataset which allowed to link certain refined parameters for the dataset (as in the parametric method of (Stinton & Evans, 2007)). Crystallite sizes were determined using the integral breadth (Lvol-IB) method.

2.7. XAS data analysis

The XANES data were analysed using ATHENA (Ravel & Newville, 2005) for absorption edge determination and spectrum normalization to an edge jump of unity using a normalization order of 2. The absorption edge position was determined as the maximum of the first derivative of the spectrum. The EXAFS data was normalized to an edge jump of unity using a normalization order of 3.

3. Results and Discussion

3.1. Data combined in operando experiments

3.1.1. $LiMn_{1.5}Ni_{0.5}O_4$ as Li-ion insertion cathode

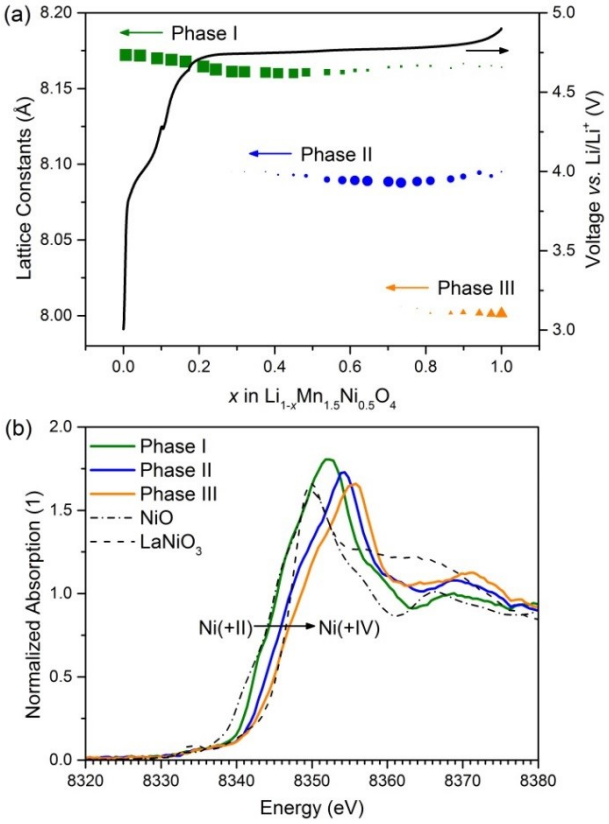

Figure 4 (a) Comparison of the voltage profile to the evolution of the cubic lattice constants of ordered $Li_{1-x}Mn_{1.5}Ni_{0.5}O_4$. The size of the symbols was scaled to the relative phase fractions. For simplicity all phases were refined in space group F*m*-3*m*. (b) Ni K-edge XANES spectra of $Li_{1-x}Mn_{1.5}Ni_{0.5}O_4$ collected at the maximum phase fraction of the corresponding phases and references.

$LiMn_{1.5}Ni_{0.5}O_4$ is a promising high potential positive electrode Li insertion material. Detailed electrochemical and structural information on ordered and disordered modifications of $LiMn_{1.5}Ni_{0.5}O_4$ can be found in our previous work (Samarasingha *et al.*, 2016). Here we present the results of an *in operando* quasi-simultaneous XRD, XANES and EXAFS study of ordered $LiMn_{1.5}Ni_{0.5}O_4$ (space group $P4_332$). A series of structural phase transitions related to the electronic changes of Ni was observed during electrochemical cycling. Fig. 4a shows the evolution of the lattice constants as well as their phase fractions compared to voltage profile and charge state. In the voltage region above 4.7 V two-phase behavior during which the unit cell dimensions remain constant while the phase fractions evolve is observed. Fig. 4b shows the Ni K-edge transmission XANES spectra of the phases (at maximum phase fraction). Initially the average Ni oxidation state is +II comparing the XANES spectra of phase **I** and NiO reference. Phase **II** is associated with an average oxidation state of +III as compared to the $LaNiO_4$ reference measurement. For phase **III** the absorption edge is shifted to higher energies compared to the Ni(+III) reference. In the lack of a Ni(+IV) reference it is therefore reasonable to assign phase **III** to a spinel structure with Ni(+IV). The reduction in lattice constants can also be explained by the decreasing ionic radii during oxidation of Ni. The slight changes in unit

cell parameters in phase **I** in the voltage range below 4.7 V could be caused by oxidation of Mn(+II) and associated decreasing ionic radii.

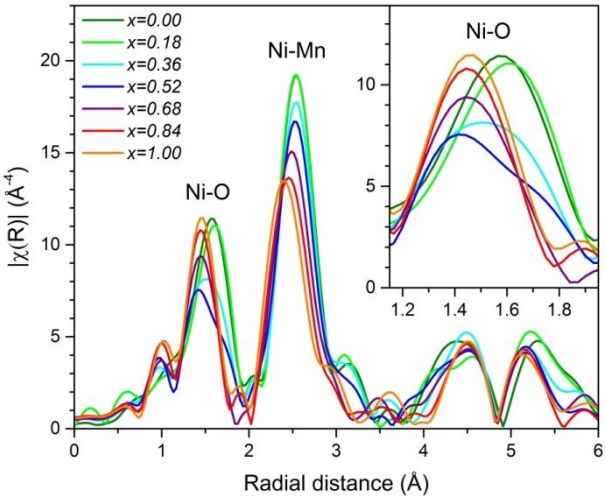

Figure 5 The radial structure function for $Li_{1-x}Mn_{1.5}Ni_{0.5}O_4$ as a function of x obtained from Fourier transformation of k^3-weighed Ni K-edge EXAFS oscillations (Δk = 3-12 $Å^{-1}$) without correcting for the phase shift.

The as-collected EXAFS spectra are shown in Fig. S3. Fourier transformation (FT) of $k^3\chi(k)$ yields the radial structure function (Fig. 5). The radial structure function provides information about the distribution and interactions between the central Ni atom and coordinating atoms. The FT was not corrected for photoelectron phase shifts, the observed bond distances might therefore appear about 0.4 Å shorter than the actual bond distances. The peaks at 1.4 and 1.6 Å represent the Ni-O interactions in the first coordination sphere. The peak at 2.5 Å corresponds to the Ni-Mn interaction in the second coordination sphere. At higher distances peaks from more distant neighbors and associated multi-scattering are observed. The peak height of the FT depends on the back-scattering of the photoelectron by the coordinated atoms. The peak height decreases if there is a distribution in distances to coordinating atoms which leads to destructive interference in the EXAFS oscillations. During the removal of 0.18 Li from $Li_1Mn_{1.5}Ni_{0.5}O_4$ the Ni-Mn coordination sphere remains unchanged while the Ni-O peak slightly decreases and shifts to higher distances. Such a slight variation in Ni-O distances might be result from oxidation of Mn(+II) to Jahn-Teller (JT) active Mn(+III) which would distort Mn-O_6 octahedra. When the structure is further delithiated Ni(+II) is oxidized to Ni(+III) and Ni(+IV). While for both Ni(+II) and Ni(+IV) equal Ni-O distances are expected, a distortion of the Ni(+III)-O_6 octahedron is likely since Ni(+III) is a low-spin JT ion. Changes in the Ni-O interaction are clearly resolved in the zoom on the corresponding peaks in the radial distribution function (inset Fig. 5). The initially single Ni-O peak splits in two which can be seen from the gradual disappearance and growing of the peaks at 1.6 Å and 1.4 Å, respectively, which confirms a stepwise reduction in Ni-O distances. At maximal phase fraction of phase **II** which was associated with JT Ni(+III) at x = 0.68 the peak at 1.6 Å is indiscernible, however, pronounced

broadening and low height suggest a distortion of the Ni(+III)-O_6 octahedron. In fully charged state (x = 1.00) the peak height and broadening are similar to the initial Ni-O peak which confirms uniform distances in the non-JT Ni(+II)-O_6 and Ni(+IV)-O_6 octahedra. Changes are also apparent in the Ni-Mn interaction. The Ni-Mn distances decrease during Ni oxidation which is consistent with the decreasing ionic radius of the Ni species. The spread in Ni-Mn distances increases throughout the charge process as indicated by the lower peak height. Furthermore, the Ni-Mn peak does not revert to its initial shape once the JT distortion is removed as observed for the Ni-O peak. This observation might be an indication of the highly instable JT Mn(+III) ions being split into more stable Mn(+II) and Mn(+IV) ions during the charge which could give rise to a spread in Ni-Mn distances but not Ni-O distances. Further quantitative analysis (*i. e.* local structure fitting) would be necessary to confirm these theories.

3.2. Bi_2S_3 as Na-ion conversion anode

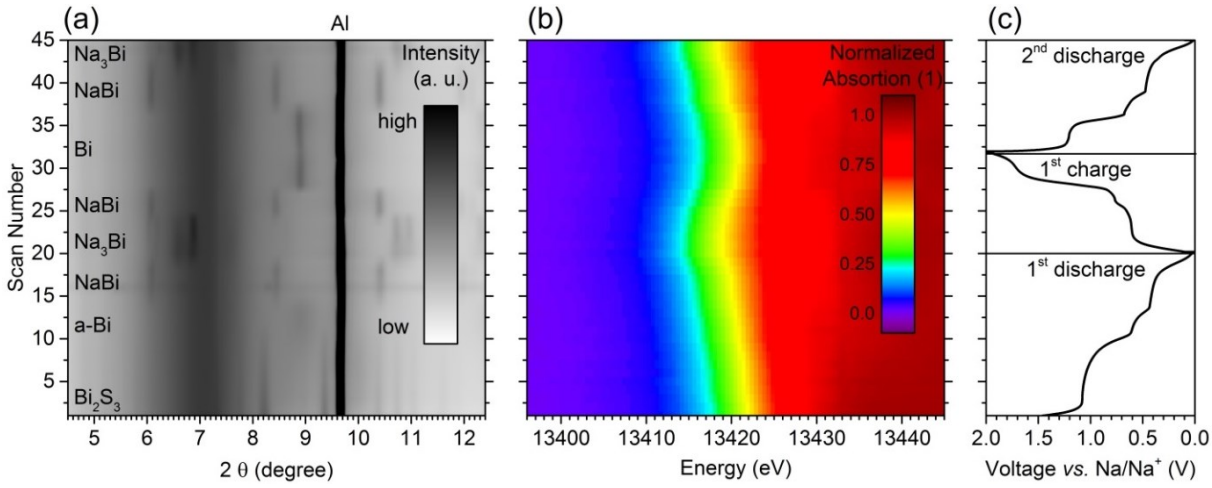

Figure 6 Film plots of the (a) diffraction profiles (λ = 0.50648 Å) and (b) Bi L3-edge XANES spectra collected quasi-simultaneously are compared to the (c) voltage profile. The data were collected at SNBL, ESRF.

Bi_2S_3 is a high capacity conversion anode material for SIBs (Li *et al.*, 2016). Fig. 6 shows the results of a combined *in operando* XRD/XANES synchrotron experiment for the first 1.5 cycles. A partially reversible redox-reaction can be assigned as follows:

$$Bi_2S_3 + 12\ Na \leftrightarrow 2\ Na_3Bi + 3\ Na_2S$$

Fig. 6a indicates that this reaction passes through various intermediate phases (Bi, NaBi and Na-S phases which were not labelled) during the electrochemical cycle. The formation of Bi_2S_3 was not fully reversible in the voltage range of 0.01 to 2 V. This is further consistent with the observed Bi L3-edge absorption energy shift from 13422.3 eV in the pristine Bi_2S_3 electrode to 13416.9 eV for the fully sodiated electrode (Na_3Bi) and back to 13421.0 eV after the first cycle which is higher than that of pure Bi metal (13419.0 eV). Analysis of a similar *in operando* XRD/XANES dataset was

demonstrated in our recent work on metallic Bi with different crystallite sizes (Sottmann, Herrmann, *et al.*, 2016).

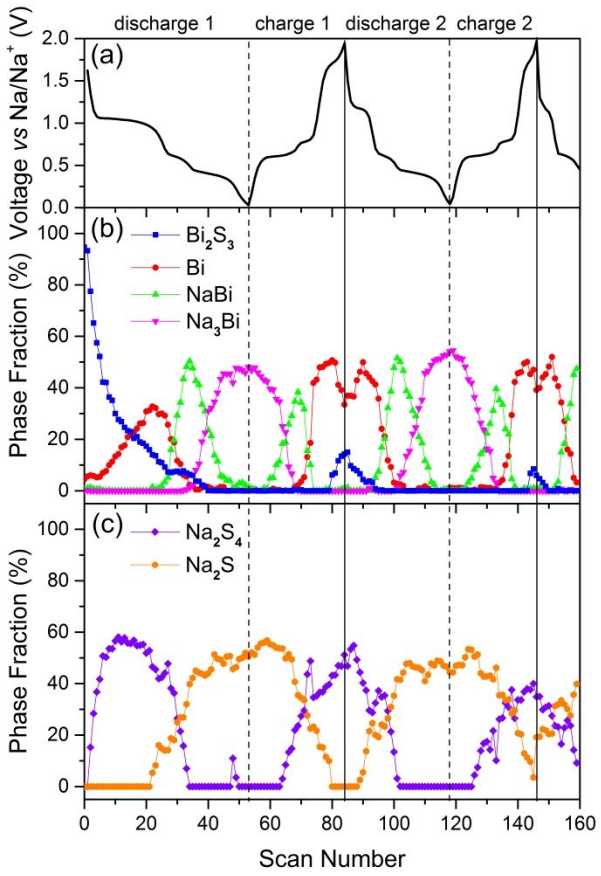

Figure 7 (a) Voltage profile of Bi_2S_3 as SIB conversion electrode compared to the phase fractions of (b) Bi_2S_3, Bi, NaBi and Na_3Bi as well as (c) Na_2S_4 and Na_2S.

Here we present the results of an *in operando* XRD structural investigation on the Bi_2S_3 SIB anode carried out in our home lab on a Bruker D8 with Mo source in transmission mode. Fig. S4 shows the series of powder patterns which is compared to the voltage profile. Fig. S5 shows the summed intensities of all powder patterns collected during the first charge and discharge, respectively, *vs.* calculated intensity and deconvoluted contributions from all phases to the calculated intensity. We used Rietveld quantitative analysis to study the phases present at different stages of electrochemical cycling. The series of powder patterns was refined in parallel as a single. Zero-shift, background (9 term Chebychev polynomial and broad background features due to amorphous material (glass fiber, carbon black, PAA, Kapton *etc.*) were fitted with a broad peak with refined position, Gaussian broadening and scale), cell parameters and peak-profile parameters for the individual phases were assumed to be constant and therefore refined to the same value for all powder patterns in the dataset. Two sets of peak-profile parameters were used for all Bi containing phases due to crystallites in the size range of 2 to 10 nm and 10 to 100 nm while Na-S phases were found with an average crystallite size in the range of 2 to 10 nm. Scale factors for the individual phases were refined for each individual

powder pattern. Despite the relatively low statistics of an individual powder pattern reliable information can be extracted due to the high number of powder patterns and the parallel refinement approach. Crystallographic details of the individual phases are presented in Table S1. Fig. 7 shows the evolution of the phase fractions of Bi_2S_3, Bi, NaBi and Na_3Bi as well as Na_2S_4 and Na_2S compared to the voltage profile for the first two cycles. Bi_2S_3 becomes nanocrystalline and the Na-Bi phases are formed from nanocrystalline Bi (a-Bi, ~ 4 nm) in the first discharge. With continued cycling the Na-Bi crystallites tend to agglomerate as exemplified for Bi in Fig. S6. The decreasing peak broadening of the Bi (0 1 2) reflection with cycle number indicates crystallite growth according to the Scherrer equation (Fig. S6a). Fig. S6b shows the change in crystallite size composition with cycling number. During the first discharge almost all Bi has a crystallite size smaller than 10 nm. After the first cycle the smaller and larger crystallite fractions are almost equal. After the second cycle the fraction of the larger crystallites dominates. The crystallite growth continues with increasing cycling number. The larger Bi particles provide less interfacial surface at which the sulfurization of Bi can take place reversibly. This can be seen as the main reason for capacity fading due to irreversibility of the Bi_2S_3 conversion reaction as evidenced by the reduction of the Bi_2S_3 phase fraction formed at the end of each cycle (Fig. 6b). It is thus crucial to maintain the metal to non-metal interface for reversible operation of conversion materials.

3.3. Cycling performance

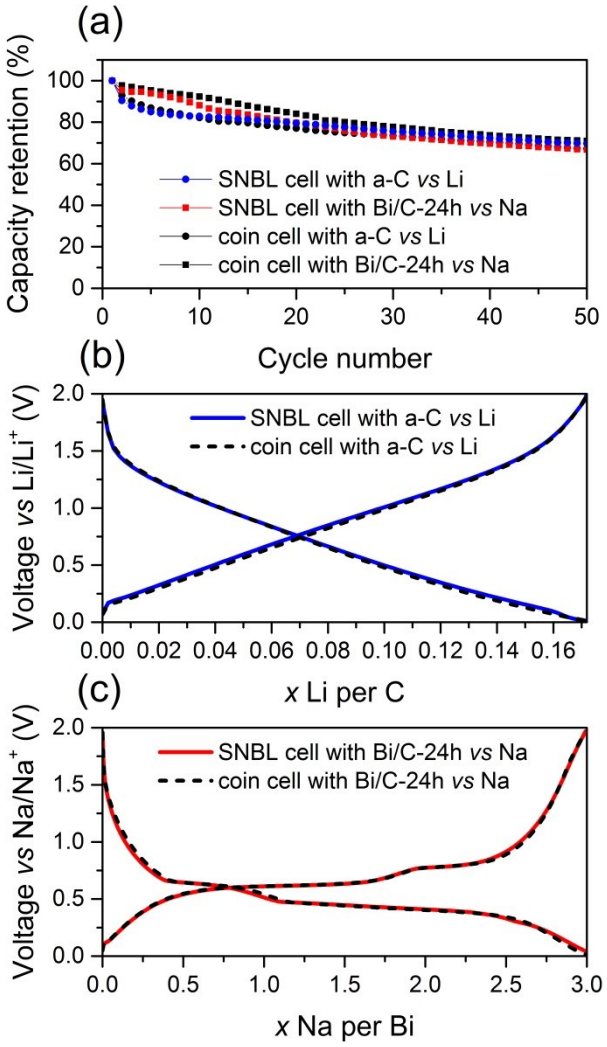

Figure 8 (a) Capacity retention of the first charge capacity during the first 50 cycles and voltage profiles, as exemplarily shown the tenth cycle, of (b) **a-C** *vs* Li/Li^+ and **Bi/C-24h** *vs* Na/Na^+ in the SNBL cell and in a reference coin cell, respectively.

Long term cycling experiments were performed on both Li and Na electrode materials in the SNBL cell as well as a coin cell (here used as a reference). For the Li cells amorphous (glassy) carbon (**a-C**) and for the Na cells nanocrystalline Bi (**Bi/C-24h**) was chosen as electrode material. The materials were synthesized and the cells were assembled as reported in (Legrain *et al.*, 2015) and (Sottmann, Herrmann*, et al.*, 2016), respectively. Fig. 8 shows that the capacity retention over 50 cycles as well as the voltage profiles obtained with the SNBL cell and the coin cell of both LIB and SIB electrodes are in good agreement. For the Li cells a current of 225 mA/g (~ C/2) and for the Na cells a current of 50 mA/g (~ C/7) was applied which resulted in total cycling durations of 1 week and 1 month, respectively, for the 50 cycles. The comparability of the cycling stability and voltage profiles in the SNBL cell and reference coin cells over periods of several weeks demonstrate the excellent hermeticity and chemical stability of the cell design.

4. Conclusions

Combined *in operando* XRD, XANES and EXAFS analysis coupled with electrochemical characterization provide a deep insight into the working mechanisms of electrode materials. An *in operando* synchrotron XRD/XAS electrochemical cell, automated sample changer and interfacing software were presented. The cell is highly hermetic, stable with respect to the chemicals used in LIB and SIB technology, robust, reusable, easy to clean, and easy to mount/change in the automated sample changer. The cells are also suitable for home lab XRD in transmission mode. The functionality of the cell was validated by investigating electronic and structural changes in the high voltage Li insertion cathode material $LiMn_{1.5}Ni_{0.5}O_4$ and the high capacity sodium conversion anode material Bi_2S_3 during cycling.

Acknowledgements We thank Geir Wiker (SNBL/ESRF, France) and Per-Olav Korsmo (University of Oslo, Norway) for help with the manufacture of the cells. We thank Staffan Ohlssen (SNBL/ESRF, France) for assistance with the software implementation. Kirill Yusenko (Swansea University, UK) and Wouter van Beek (SNBL/ESRF, France) for fruitful discussions. We thank Pushpaka Samarasingha for providing the LMNO sample and Amund Ruud and Matthias Herrmann (University of Oslo, Norway) for assistance with data collection. We acknowledge use of the EC-lab at ESRF and of the Norwegian national infrastructure for X-ray diffraction and Scattering (RECX). This work was supported by the synchrotron and neutron travel grant (Research Council of Norway, No. 216625).

References

Abdala, P. M., Mauroy, H. & van Beek, W. (2014). *J. Appl. Crystallogr.* **47**, 449-457.

Amalraj, S. F. & Aurbach, D. (2011). *J. Solid State Electrochem.* **15**, 877-890.

Asahina, H., Kurotaki, M., Yonei, A., Yamaguchi, S. & Mori, S. (1997). *J. Power Sources* **68**, 249-252.

Ashiotis, G., Deschildre, A., Nawaz, Z., Wright, J. P., Karkoulis, D., Picca, F. E. & Kieffer, J. (2015). *J. Appl. Crystallogr.* **48**, 510-519.

Baehtz, C., Buhrmester, T., Bramnik, N. N., Nikolowski, K. & Ehrenberg, H. (2005). *Solid State Ionics* **176**, 1647-1652.

Balasubramanian, M., Sun, X., Yang, X. Q. & McBreen, J. (2001). *J. Power Sources* **92**, 1-8.

Berg, E. J., Villevieille, C., Streich, D., Trabesinger, S. & Novák, P. (2015). *J. Electrochem. Soc.* **162**, A2468-A2475.

Bleith, P., van Beek, W., Kaiser, H., Novák, P. & Villevieille, C. (2015). *J. Phys. Chem. C* **119**, 3466-3471.

Borkiewicz, O. J., Shyam, B., Wiaderek, K. M., Kurtz, C., Chupas, P. J. & Chapman, K. W. (2012). *J. Appl. Crystallogr.* **45**, 1261-1269.

Borkiewicz, O. J., Wiaderek, K. M., Chupas, P. J. & Chapman, K. W. (2015). *The Journal of Physical Chemistry Letters* **6**, 2081-2085.

Brant, W. R., Schmid, S., Du, G., Gu, Q. & Sharma, N. (2013). *J. Power Sources* **244**, 109-114.

Braun, A., Shrout, S., Fowlks, A. C., Osaisai, B. A., Seifert, S., Granlund, E. & Cairns, E. J. (2003). *Journal of Synchrotron Radiation* **10**, 320-325.

Dahn, J. R., Py, M. A. & Haering, R. R. (1982). *Can. J. Phys.* **60**, 307-313.

Deb, A., Bergmann, U., Cairns, E. J. & Cramer, S. P. (2004). *Journal of Synchrotron Radiation* **11**, 497-504.

Deb, A., Bergmann, U., Cramer, S. P. & Cairns, E. J. (2007). *J. Electrochem. Soc.* **154**, A534-A541.

Dominko, R., Arčon, I., Kodre, A., Hanžel, D. & Gaberšček, M. (2009). *J. Power Sources* **189**, 51-58.

Farley, N. R. S., Gurman, S. J. & Hillman, A. R. (1999). *Electrochem. Commun.* **1**, 449-452.

Fleischmann, M., Oliver, A. & Robinson, J. (1986). *Electrochim. Acta* **31**, 899-906.

Frenkel, A. I., Yevick, A., Cooper, C. & Vasic, R. (2011). *Annual Review of Analytical Chemistry* **4**, 23-39.

Gérand, B., Blyr, A., Du Pasquier, A., Leriche, J. B. & Seguin, L. (1999). *J. Power Sources* **81–82**, 922-924.

Giorgetti, M. (2013). *ISRN Materials Science* **2013**, 22.

Gustafsson, T., Thomas, J. O., Koksbang, R. & Farrington, G. C. (1992). *Electrochim. Acta* **37**, 1639-1643.

Harks, P. P. R. M. L., Mulder, F. M. & Notten, P. H. L. (2015). *J. Power Sources* **288**, 92-105.

Herklotz, M., Scheiba, F., Hinterstein, M., Nikolowski, K., Knapp, M., Dippel, A.-C., Giebeler, L., Eckert, J. & Ehrenberg, H. (2013). *J. Appl. Crystallogr.* **46**, 1117-1127.

Herklotz, M., Weiss, J., Ahrens, E., Yavuz, M., Mereacre, L., Kiziltas-Yavuz, N., Drager, C., Ehrenberg, H., Eckert, J., Fauth, F., Giebeler, L. & Knapp, M. (2016). *J. Appl. Crystallogr.* **49**, 340-345.

Hu, Y.-Y., Liu, Z., Nam, K.-W., Borkiewicz, O. J., Cheng, J., Hua, X., Dunstan, M. T., Yu, X., Wiaderek, K. M., Du, L.-S., Chapman, K. W., Chupas, P. J., Yang, X.-Q. & Grey, C. P. (2013). *Nat Mater* **12**, 1130-1136.

Ito, A., Sato, Y., Sanada, T., Hatano, M., Horie, H. & Ohsawa, Y. (2011). *J. Power Sources* **196**, 6828-6834.

Legrain, F., Sottmann, J., Kotsis, K., Gorantla, S., Sartori, S. & Manzhos, S. (2015). *J. Phys. Chem. C* **119**, 13496-13501.

Leriche, J. B., Hamelet, S., Shu, J., Morcrette, M., Masquelier, C., Ouvrard, G., Zerrouki, M., Soudan, P., Belin, S., Elkaïm, E. & Baudelet, F. (2010). *J. Electrochem. Soc.* **157**, A606-A610.

Li, W.-J., Han, C., Chou, S.-L., Wang, J.-Z., Li, Z., Kang, Y.-M., Liu, H.-K. & Dou, S.-X. (2016). *Chemistry – A European Journal* **22**, 590-597.

Lowe, M. A., Gao, J. & Abruna, H. D. (2013). *J. Mater. Chem. A* **1**, 2094-2103.

Lv, D., Bai, J., Zhang, P., Wu, S., Li, Y., Wen, W., Jiang, Z., Mi, J., Zhu, Z. & Yang, Y. (2013). *Chem. Mater.* **25**, 2014-2020.

Marco, R. D. & Veder, J.-P. (2010). *TrAC, Trends Anal. Chem.* **29**, 528-537.

McBreen, J. (2008). *J. Solid State Electrochem.* **13**, 1051-1061.

McBreen, J., Mukerjee, S., Yang, X. Q., Thurston, T. R. & Jisrawi, N. M. (1997). *Second International Symposium on New Materials for Fuel Cells and Modern Battery Systems* edited by O. Savadogo & P. R. Roberge, pp. 348 -358. Ecole Polytechnique, Montreal (Quebec) Canada

McBreen, J., O'Grady, W. E., Pandya, K. I., Hoffman, R. W. & Sayers, D. E. (1987). *Langmuir* **3**, 428-433.

Morcrette, M., Chabre, Y., Vaughan, G., Amatucci, G., Leriche, J. B., Patoux, S., Masquelier, C. & Tarascon, J. M. (2002). *Electrochim. Acta* **47**, 3137-3149.

Nakai, I., Shiraishi, Y. & Nishikawa, F. (1999). *Spectrochimica Acta Part B: Atomic Spectroscopy* **54**, 143-149.

Nelson Weker, J. & Toney, M. F. (2015). *Adv. Funct. Mater.* **25**, 1622-1637.

Nikolowski, K., Baehtz, C., Bramnik, N. N. & Ehrenberg, H. (2005). *J. Appl. Crystallogr.* **38**, 851-853.

Novák, P., Panitz, J. C., Joho, F., Lanz, M., Imhof, R. & Coluccia, M. (2000). *J. Power Sources* **90**, 52-58.

Palomares, V., Serras, P., Villaluenga, I., Hueso, K. B., Carretero-Gonzalez, J. & Rojo, T. (2012). *Energy Environ. Sci.* **5**, 5884-5901.

Permien, S., Indris, S., Schürmann, U., Kienle, L., Zander, S., Doyle, S. & Bensch, W. (2016). *Chem. Mater.* **28**, 434-444.

Peterson, V. K. & Papadakis, C. M. (2015). *IUCrJ* **2**, 292-304.

Ravel, B. & Newville, M. (2005). *Journal of Synchrotron Radiation* **12**, 537-541.

Rhodes, K., Kirkham, M., Meisner, R., Parish, C. M., Dudney, N. & Daniel, C. (2011). *Rev. Sci. Instrum.* **82**, 075107.

Richard, M. N., Koetschau, I. & Dahn, J. R. (1997). *J. Electrochem. Soc.* **144**, 554-557.

Ronci, F., Scrosati, B., Albertini, V. R. & Perfetti, P. (2000). *Electrochem. Solid-State Lett.* **3**, 174-177.

Ronci, F., Scrosati, B., Albertini, V. R. & Perfetti, P. (2001). *The Journal of Physical Chemistry B* **105**, 754-759.

Rosciano, F., Holzapfel, M., Kaiser, H., Scheifele, W., Ruch, P., Hahn, M., Kotz, R. & Novak, P. (2007). *Journal of Synchrotron Radiation* **14**, 487-491.

Samarasingha, P. S., Sottmann, J., Margadonna, S., Nilsen, O. & Fjellvåg, H. (2016). *submitted*

Sharma, N., Pang, W. K., Guo, Z. & Peterson, V. K. (2015). *ChemSusChem* **8**, 2826-2853.

Shen, Y., Pedersen, E. E., Christensen, M. & Iversen, B. B. (2014). *Rev. Sci. Instrum.* **85**, 104103.

Shin, H. C., Park, S. B., Jang, H., Chung, K. Y., Cho, W. I., Kim, C. S. & Cho, B. W. (2008). *Electrochim. Acta* **53**, 7946-7951.

Shui, M., Zheng, W., Shu, J., Wang, Q., Gao, S., Xu, D., Chen, L., Feng, L. & Ren, Y. (2012). *Mater. Res. Bull.* **47**, 2455-2459.

Slater, M. D., Kim, D., Lee, E. & Johnson, C. S. (2013). *Adv. Funct. Mater.* **23**, 947-958.

Sottmann, J., Bernal, F. L. M., Yusenko, K. V., Herrmann, M., Emerich, H., Wragg, D. S. & Margadonna, S. (2016). *Electrochim. Acta* **200**, 305-313.

Sottmann, J., Herrmann, M., Vajeeston, P., Hu, Y., Ruud, A., Drathen, C., Emerich, H., Fjellvåg, H. & Wragg, D. S. (2016). *Chem. Mater.*

Stinton, G. W. & Evans, J. S. O. (2007). *J. Appl. Crystallogr.* **40**, 87-95.

Tang, M., Carter, W. C. & Chiang, Y.-M. (2010). *Annual Review of Materials Research* **40**, 501-529.

Tarascon, J. M. & Armand, M. (2001). *Nature* **414**, 359-367.

Villevieille, C., Sasaki, T. & Novak, P. (2014). *RSC Advances* **4**, 6782-6789.

Wilson, B. E., Smyrl, W. H. & Stein, A. (2014). *J. Electrochem. Soc.* **161**, A700-A703.

Yamamoto, K., Minato, T., Mori, S., Takamatsu, D., Orikasa, Y., Tanida, H., Nakanishi, K., Murayama, H., Masese, T., Mori, T., Arai, H., Koyama, Y., Ogumi, Z. & Uchimoto, Y. (2014). *J. Phys. Chem. C* **118**, 9538-9543.

Supporting information

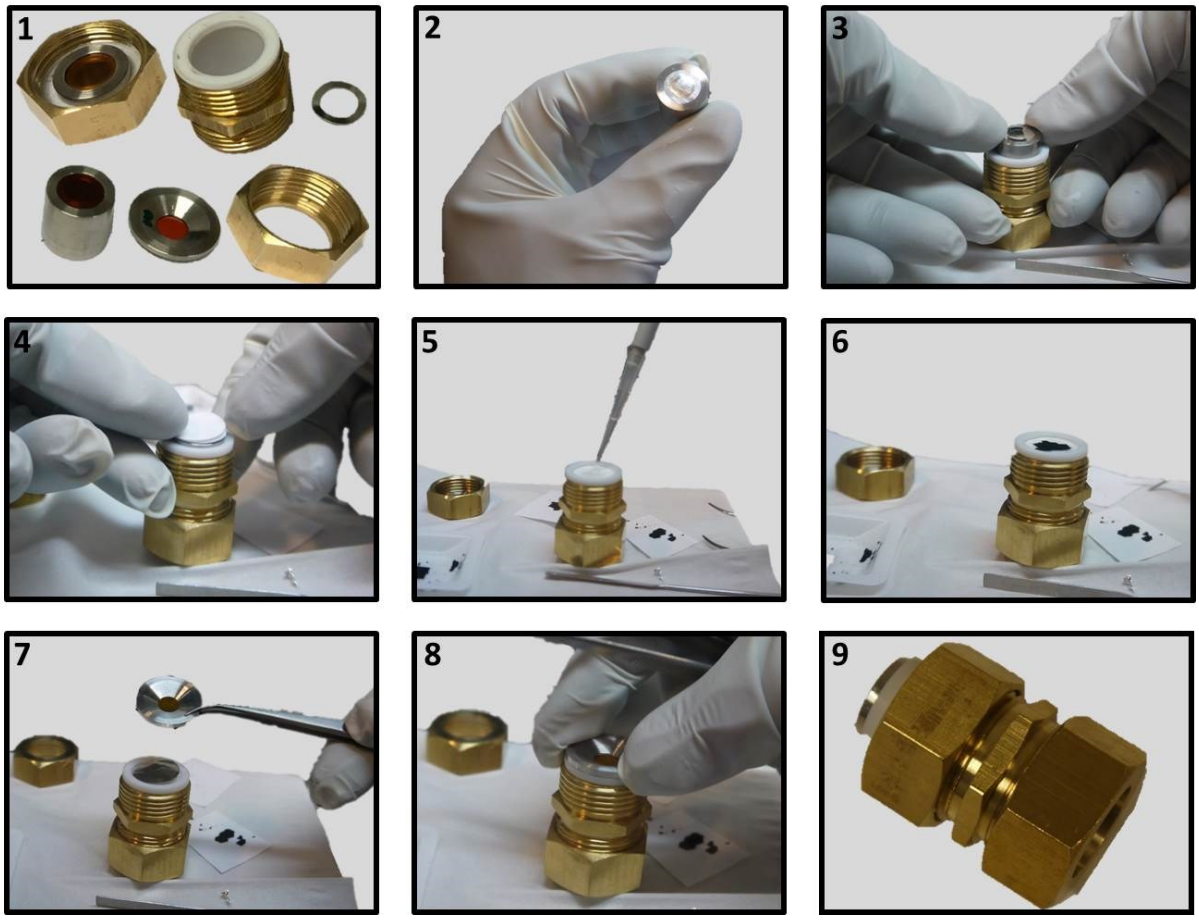

Figure S1 Assembly procedure: (1) Various parts of the cell shown in the assembling order; piston **C**, Teflon cylinder **T**, spring, piston **B**, battery as show in (2) to (7) and finally piston **A**; (2) Na or Li metal spread on piston **B**; (3) piston **B** placed in Teflon cylinder **T** on top of piston **C** and a spring; (4) glass fiber separator; (5) electrolyte; (6) self-standing electrode; (7) metal foil (or electrode coated on metal foil); (8) piston **A**; (9) closed cell.

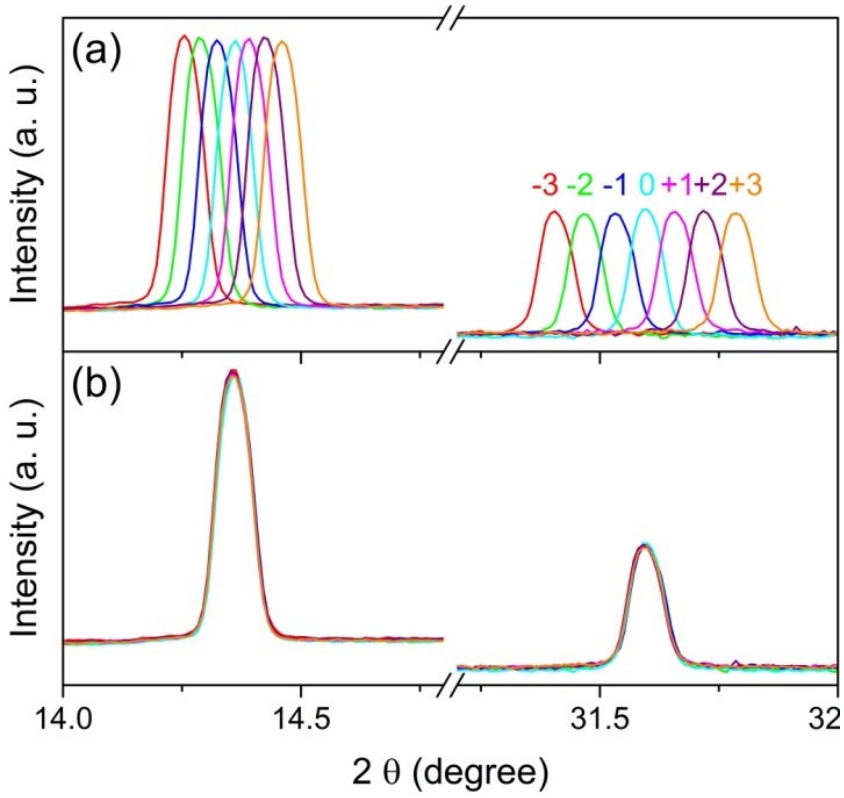

Figure S2 (a) Diffraction profiles (λ = 0.50648 Å) of Al foil in a cell mounted in the center of the diffractometer (zero position) and displaced in 1 mm steps in the range of ±3 mm from the center and (b) corrected for the displacement error prior to data reduction with pyFAI (Ashiotis *et al.*, 2015). For this purpose the distance parameter was modified iteratively in pyFAI (here by -3, -2, -1, +1, +2 and +3 mm) until the Al peak of the cell in zero and displaced positions matched.

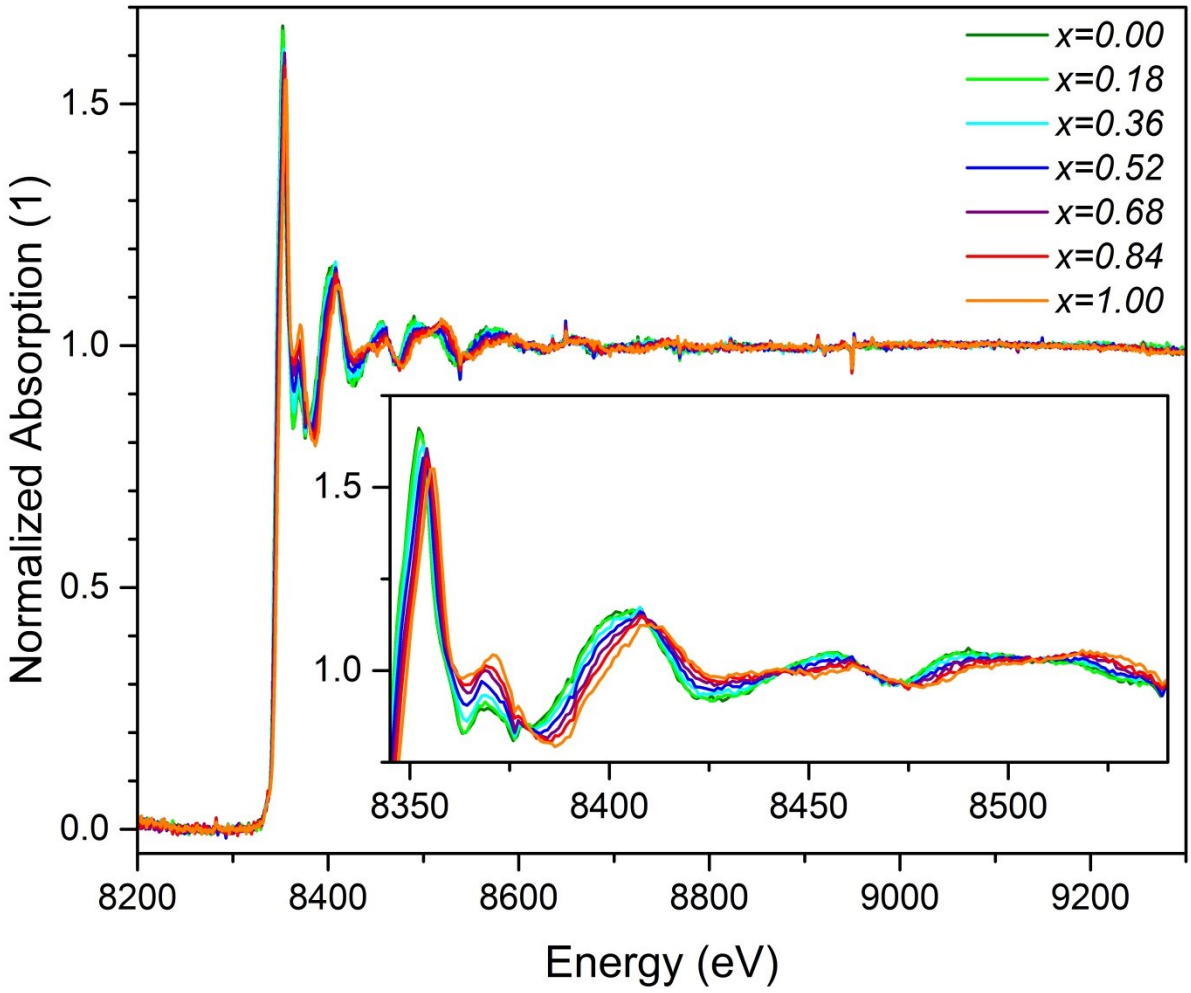

Figure S3 Normalized EXAFS spectra of $Li_{1-x}Mn_{1.5}Ni_{0.5}O_4$ as a function of x.

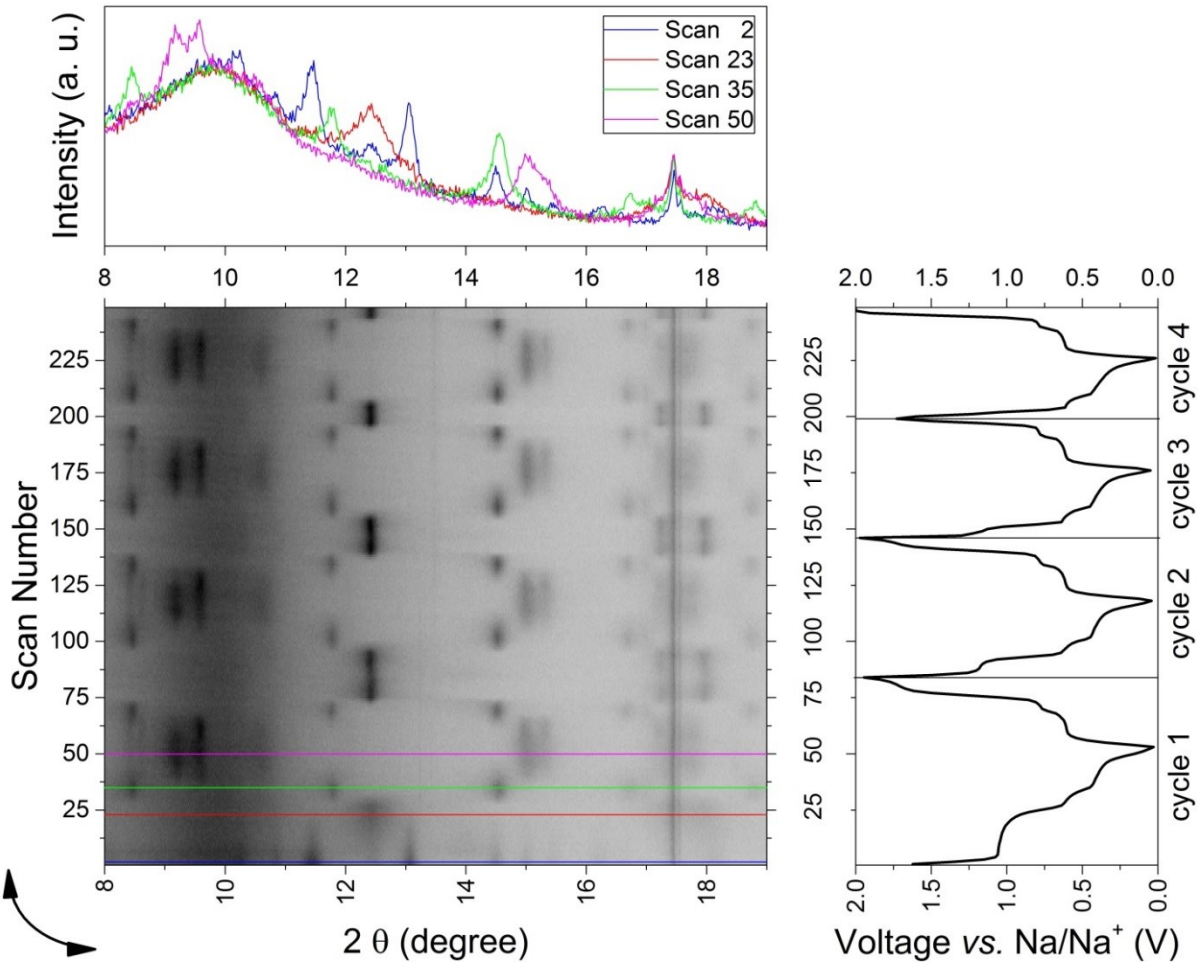

Figure S4 *In operando* XRD data collected Bi_2S_3 as Sib anode using a Bruker D8 with Mo source in transmission mode Bi_2S_3. The dark color in the film plots corresponds to high intensities.

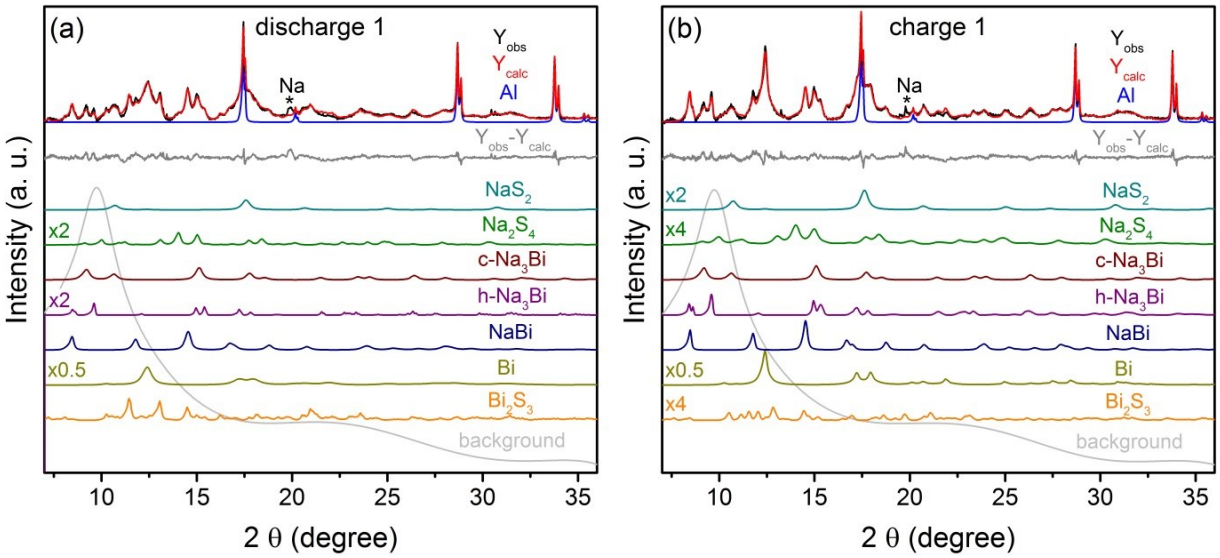

Figure S5 Summed intensities of all powder patterns collected during the first charge (a) and discharge (b), respectively, *vs.* calculated intensity and deconvoluted contributions from all phases to the calculated intensity. The background is represented as the light gray line.

Table S1 Crystallographic details of the Na-Bi-S system.

phase	space group, structure	a (Å)	b (Å)	c (Å)	crystallite size 1 (nm)	crystallite size 2 (nm)
Bi_2S_3	*Pbnm* (62), Sb_2S_3	11.15	11.27	3.98	3	56
Bi	*R*-3*m* (166), As	4.54	a	11.84	4	23
NaBi	*P4/mmm* (123), AuCu	3.45	a	4.79	3	21
h-Na_3Bi	*P*6_3*/mmc* (194), Na_3As	5.44	a	9.65	-	63
c-Na_3Bi	*Fm*-3*m* (225), Li_3Bi	7.65	a	a	-	63
Na_2S_4	I-42d (122), Na_2S_4	9.55	a	11.73	4	-
Na_2S	*Fm*-3*m* (225), Fluorite-CaF_2	6.58	a	a	4	-

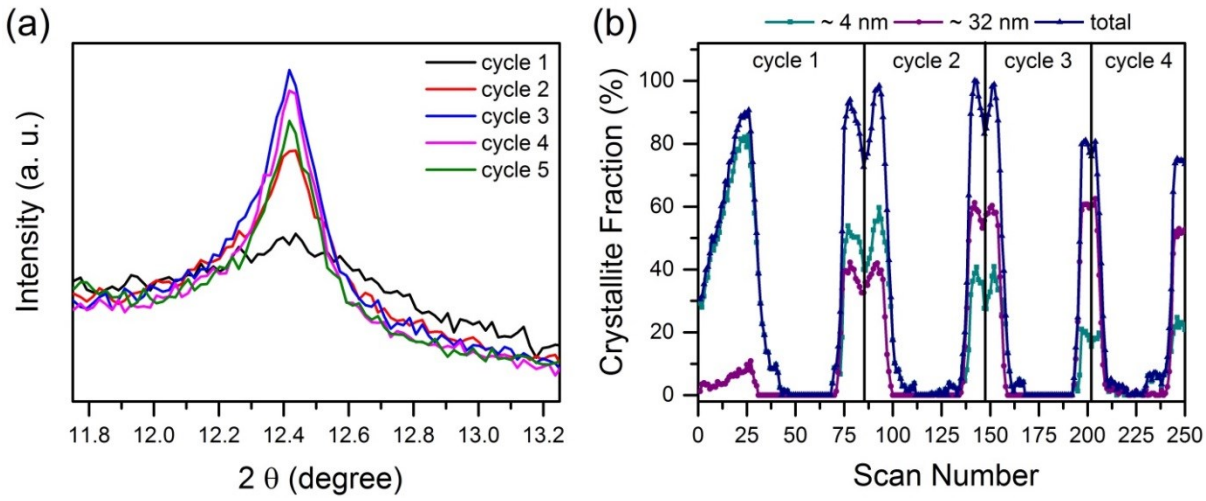

Figure S6 Bi (0 1 2) peak broadening *vs*. cycle number (Mo radiation). Evolution of the crystallite size distribution during the first 4 cycles.